The Effect of Thin Film Adhesives on Mode II Interlaminar Fracture Toughness in Carbon Fiber Composites with Shape Memory Alloy Inserts

Derek J. Quade[1,2*], Sadhan C. Jana[1], Gregory N. Morscher[1], Manigandan Kanaan[1], Linda McCorkle[3]

[1] *The University of Akron*

[2] *NASA Glenn Research Center*

[3] *Ohio Aerospace Institute*

Abstract

A single sheet of nickel-titanium (NiTi) shape memory alloy (SMA) was introduced within an IM7/8552 polymer matrix composite (PMC) panel in conjunction with multiple thin film adhesives to promote the interfacial bond strength between the SMA and PMC. End notched flexure (ENF) testing was performed in accordance to ASTM D7905 method for evaluation of mode II interlaminar fracture toughness (G_{IIC}) of unidirectional fiber-reinforced polymer matrix composites. Acoustic emissions (AE) were monitored during testing with two acoustic sensors attached to the specimens. The composite panels examined using scanning electron microscopy techniques after part failure. G_{IIC} values for the control composite samples were found to be higher than those of samples with embedded SMA sheets. The presence of adhesives bonded to SMA sheets further diminished the G_{IIC} values. AE values revealed poor bonding of the panels, with little to no signals during testing.

Keywords: Shape Memory Alloy; Polymer Matrix Composite, End Notched Flexure, Thin Film Adhesives

1. Introduction

The fabrication and testing of hybrid materials of SMA and PMC have been a growing area of research interest in the past decade. Such research studies include debonding of NiTi wires from composites of carbon fiber[1] and epoxy systems[2-4] and NiTi strips embedded in specimens for thermomechanical testing[4,5]. SMA inclusion into chevrons[6] as well as systems designed to test their response from bending[7] and buckling[8] within composites has been reported. Modeling of SMAs within composite systems has been attempted[9,10]. The SMAs ability to induce large amounts of stress from heating while embedded within polymers has opened a new area of interest on hybrid actuators[11-13]. In order to advance this technology properly, further testing is required to fully understand and optimize the bonds between these dissimilar materials.

The root of this type of actuator depends on the physical properties of the SMA itself. The SMA is able to generate large amounts of stress when constricted through reversible, thermoelastic martensitic transitions of the crystalline structures[14]. Austenitic crystals shift to a variety of martensitic

*Corresponding Author

structures during times of loading or heating. This shift is directly responsible for the aforementioned stresses generated when constricted, as is the case when embedded within a composite[15]. The bending and flex that occur within an SMA-PMC actuator system depend highly on the interlaminar strength between the individual materials.

Prior investigations involving SMA inclusion within composites focused on the modeling of the actuator stresses[6,11], enhancing the bond between metal and polymer[1-4,10], or construction of a NiTi based actuator system[6-8,10,12]. The majority these studies utilize optically clear materials[2-12] comprised of glass/aramid fibers and optically clear resins. Within these systems, stresses and debonding can be monitored with optical methods, such as Raman spectroscopy. Limited studies investigate the interactions between SMAs and PMCs that are not optically clear, typically involving carbon fiber reinforced polymer (CFRP)[1,16,17].

The goal of this research was to assess the effects of thin film adhesives on the interlaminar strength between an SMA and PMC in an actuator. A series of 22-ply unidirectional composite panels were fabricated. Two of the three SMA panels included additional thin film adhesive between the SMA and PMC in order to optimize bonding. Modified 3-point bend testing was performed in accordance to ASTM standard D7905: Standard Test Method for Determination of the Mode II interlaminar fracture toughness of unidirectional fiber-reinforced polymer matrix composites[18]. During testing, two acoustic sensors were attached to the specimens to monitor acoustic emissions. AE was used in order to provide a method of detecting debonding within specimens during interlaminar failure, a process that is usually monitored in prior research using visual methods.

2. Experimental Techniques

2.1. PMC Panel Layup

PMC panel layup was based on ASTM Method D7905[18]. PMC panels of an average thickness of 3.55 mm were fabricated by organizing twenty-two panels with 0° unidirectional plies. This structure is schematically shown in Figure 1. Of these, eleven (11) plies of material were put on either side of a single sheet of SMA material. A non-stick insert is placed between the SMA and PMC as a “pre-crack” in the test specimen. The control materials were fabricated with no SMA or with no adhesives, but contained the “pre-crack” per the standard.

2.2. Materials and Fabrication

Flat annealed NiTi sheets were supplied by Johnson Matthey (San Jose, California), measuring 457.2 mm in length, 101.6 mm in width, and 0.127 mm in thickness. The SMA strips were cut into rectangular specimens, 152.4 mm long and 101.6 mm wide. The SMA specimens were wiped with acetone and dried before inserting in the PMC. The PMC used was a HexPly 8552 Epoxy Matrix embedded with IM7 carbon fibers obtained from Hexcel (Salt Lake City, Utah)[19]. For control samples, no adhesive was placed between the NiTi section and PMC. The rest of the samples were bonded using Hysol EA9696[20] (Bay Point, California) and Cytec FM 377U[21] (Olean, New York) thin film adhesives. The pre-crack insert used for this testing was a thin polyimide film, measuring 0.0127 mm in thickness, 25.4

mm in width, and 55.88 mm in length. A mold release agent was coated onto the insert and heated to 200° C for 1 hour in order to prevent the bonding of the PMC with the insert.

The composite specimens were assembled into panels of dimension 152.4 mm x 152.4 mm according to the lay-up guidelines presented in Figure 1. The panels were processed in an autoclave according to the required procedure for the HexPly 8552[19]. The panels were first cured for 1 hour at 110° C under full vacuum and a pressure of 0.1 MPa. The temperature was then ramped up to 176° C and vacuum vented when the pressure increased beyond 0.2 MPa to a total pressure of 0.68 MPa for 2 hours. After curing, each panel was cut into 25.4 mm wide and 152.4 mm long specimens for conducting tests. The edges of the specimens were coated in white spray paint to assist in the visual detection of the delamination tip and in making compliance calibration markings. Four marks were placed on the specimens; one to mark the tip of the insert, and three placed at distances of 20, 30, and 40 mm from the tip of the insert.

2.3. Mechanical Testing

Tests were conducted on an Instron 5582 testing device running the Bluehill V 2.0 software suite. Two acoustic sensors were attached to the specimens at the end opposite of the crack insert, on opposing sides of the bottom support roller. Vacuum grease was used to maintain contact with the specimen while the clips held the sensors to the specimen. The acoustic sensors were connected to a Digital Wave (Huntingdon Valley, PA) preamplifier, which in turn was connected to a computer running the WaveExplorer (Huntingdon Valley, PA) software suite. AE sampling rate was 10 MHz, while 2048 data points for each waveform was recorded which also included 512 data points per trigger points. Lead break tests were performed on the specimens before the test to make sure the AE sensors were in the correct locations and functioning properly. An end-notched flexure (ENF) setup was used for testing. The ENF test involves loading a sample in three-point bending with a mid-plane starter crack at the left end, indicated by the distance (a_i). This test setup is shown in Figure 2.

The crack length (a_0) was initially measured from the support roller with a half-span length L spanning the distance from the support rollers to the center loading roller. A compliance calibration (CC) test was performed in order to find the relationship between specimen compliance and crack length. Three loadings were used to obtain three plots of compliances versus crack length. The first two loadings used a load below failure to prevent delamination. For the first load, the specimen was positioned in the three-point-bend fixture with the left bottom-roller support below the 20 mm mark. A load and unload sequence was applied to acquire compliance for the specimen. This procedure was repeated, shifting the specimen so the bottom support-roller would be positioned below the 40 mm and subsequently 30 mm mark. At the 30 mm mark, the specimen was loaded until the crack extended and then load was removed.

A duo of acoustic sensors was attached to each specimen during testing. As the specimens were tested, acoustic events were recorded and marked at each point it occurred. Before the start of each test, pencil lead breaks (0.5 mm diameter) were performed at the edge of the samples so that the sound traveled across both sensors. The time difference of arrival between the sensors was monitored for the

first peak (extensional mode). From these peaks, the speed of sound across the specimens was calculated by the distance between the two sensors (x) divided by the difference in arrival time (Δt_x).

Optical microscopy was performed on an Olympus Microscope DFC295 utilizing the Leica Applications Suite software, while scanning electron microscopy was performed on a Hitachi S-4700 electron microscope.

3. Results

The analysis of data yielded information on fracture toughness. The acoustic emissive energy signals recorded at the time of experiments were added to load vs. extension graphs to facilitate data interpretation.

3.1. Mechanical Results

Mechanical tests were performed via the compliance calibration method. For this method, the specimen was "flexed" in two different locations before crack propagation was progressed at a third location. These three loadings were applied to generate three plots of compliances versus crack length for each specimen. Both the load and unload sequences were recorded within the Bluehill software suite. The results of this testing are shown below for each specimen in Figures 3-6.

The four different graphs for each figure indicate the individual specimens which made up each test group (four specimens for control, four specimens for SMA group, etc). The graphs shown in Figure 3 show distinctly different slopes of the three different compliances used, which is typical of a composite system. The addition of SMA (with and without system) shows a difference in that the slopes of the different compliances are all very close in relation to each other. This shows the effect that the inner SMA ply has on the total flex of the system. Overall, Figures 4-6 shows that the flex of the system is not only increased by the addition of SMA, but is normalized no matter where the compliance of the system is loaded at (A20, A30, or A40).

3.2. Acoustic Emission Results

Acoustic signals generated during DCB testing were recorded by the WaveExplorer software via the acoustic sensors and preamplifier. Cumulative AE are plotted alongside the load data for each of the test specimens to better correlate acoustic signals originating from the mechanical events. Acoustic events were only detected during the crack propagation phase; such data are presented in Figures 7-10.

For the majority of graphs seen in Figures 7-10, a minimal amount of acoustic energy is detected within the ENF system during testing. This indicates that the mechanism of failure in these specimens (despite propagating a crack) cannot necessarily be detected and tracked via acoustic emissions.

3.3 Microscopy Results

The effect of the SMA inserts and adhesives on the ENF test results was evaluated by examining scanning electron microscopy images. SEM images were taken of the area in which the pre-crack insert was placed, along with the area in which crack propagation occurred. Figure 11 shows the pre-crack and crack propagation area of specimen 1-1.

There is a noticeable difference in the debond area where the insert was compared to where actual crack propagation progressed through the control specimen. This includes not only a rougher surface, but broken fibers and matrix areas as well. Figure 12 shows similar images for specimen 2-2, the specimen with SMA and no added adhesive.

In these images, the surface roughness between pre-crack and crack sections is readily recognized by the transition from smooth crack to rough. Comparing this image to that in Figure 11, the crack propagation section for the SMA control sample conformed to the shape of the SMA material and did not progress through any plies of the PMC itself; this is the reason why the surface is smoother and without any noticeable fiber breaks. The distinct pattern seen in image B of Figure 12 is actually that of the PMC when conformed against the SMA material).

Figure 13 shows the pre-crack and crack propagation section of specimen 3-2, the ENF specimen that utilized the FM adhesive between PMC and SMA.

Similar to Figure 12, the images in Figure 13 show the difference in surface roughness between the pre-crack area of the specimen (where the insert was) when compared to the crack section of the specimen. Unlike the control specimen, however, this specimen shows signs of adhesive in image B of Figure 13. While an imprint of the SMA material is seen, sections of image B (Figure 13) show various cracks/delaminations between the SMA imprint and adhesive. This shows that the majority of FM adhesive remained alongside the PMC during ENF testing, while actively debonding from the SMA during the test.

Figure 14 shows the pre-crack and crack propagation section of specimen 4-1, the ENF specimen that utilized Hysol adhesive between PMC and SMA.

Again, we note the difference in surface roughness between the pre-crack area of the specimen (where the insert was) against the crack section of the specimen. Unlike Figure 13, however, the specimen with Hysol as the adhesive shows an even higher extent of bonding with the PMC layer. This is seen in image B of Figure 14, where little to no ridges or delaminations are seen in the images taken. This indicates that little to no material stayed adhered to the SMA during the ENF testing.

4. Analysis

The results from ENF testing was analyzed in order to highlight the differences in interlaminar strengths between the sets of specimens. This analysis includes a compliance calibration overview of the samples, which then leads to G_{IIC} values for each of the specimens.

4.1 Compliance Calibration

The compliance calibration (CC) method was performed on the NPC fracture tests. This method involves loading the specimens at different crack lengths in order to obtain a value of compliance from each test. Figure 15 shows a typical ENF load-displacement plot from NPC fracture test specimen 1-3.

For each crack length, a value of compliance was determined by a least-squares linear regression analysis of the data to obtain the slope of the displacement versus load data. The compliances found were plotted against the corresponding tested compliance length distances (A20, A30, A40) raised to the third power and fit to a line via Equation 1.

$$C = A + ma^3 \quad (1)$$

Figure 16 shows a fit of Equation 1 with the experimental data, where compliance is plotted against the crack value for each plot in Figure 15.

The resulting values from Equation 1 were used to find the value of mode II interlaminar fracture toughness, G_{IIC}. This toughness value is determined using Equation 2.

$$\mathbf{G_{IIC}} = \frac{\mathbf{3mP_{max}^2 a_0^2}}{\mathbf{2B}} \quad (2)$$

In Equation 2, G_{IIC} is the mode II interlaminar fracture toughness, m is the CC coefficient, P_{max} is the maximum force from fracture testing, a_0 is the crack length used for the fracture test (30 mm), and B is the specimen width.

The average G_{IIC} values from each specimen series were summarized for comparative analysis in Figure 17. Variation in calculated G_{IIC} values resulted in large standard deviations for the control series. Standard deviations were lower for specimens with embedded SMA. This is attributed to variation within specimens during fabrication and testing.

5. Discussion

Calculated G_{IIC} results from this study were significantly lower than G_{IIC} values found in literature[18,22]. G_{IIC} values from this study averaged 2.46 $^{in\text{-}lbf}/_{in^2}$. ASTM interlaboratory studies[18] G_{IIC} values were 5.18 $^{in\text{-}lbf}/_{in^2}$, while independent research by O'Brien[22] found G^{IIC} values of 6.5 $^{in\text{-}lbf}/_{in^2}$. Analysis of difficulties during our study can reveal why results found were lower than those found by previous researchers

5.1.1. ENF Background

The end notched flexure method was developed in the late 1970's by Barrett and Foschi[23]. This was later adapted by Russel and Street[24], who developed the earliest analytical expressions for mode II strain energy release rate (GII) and specimen compliance. Subsequently, derivation of expressions of G_{IIC} for a variety of test methods was proposed. These include three-point bending[23], four-point bending [25], end-loaded split[26], and tapered end-notched flexure methods[27]. The departure from 3-point bending test was driven by the following rationale - the crack propagation seen in 3-point bending tests for obtaining G_{IIC} values is unstable leading to generation of only one data point per test, as opposed to the multiple G_{IC} values generated from a single DCB test. A number of research papers[28-38] have all stated this issue and looked to correct, or better estimate fracture toughness values from 3-point bending ENF tests.

Aside from irregular crack growth propagation, other issues in ENF testing have also been found including specimen thickness/curing pressure[37], bending rotations[35], nonlinear interface fracture[32], process zone phenomenon[30], and even the friction between the loading pin and the ENF specimen[33]. Any one of these variables, along with those generated from the insertion of an SMA into the specimen, can be the cause of such low G_{IIC} values within tested specimens. There were specific examples of issues that arose during testing that may be attributed to these low values.

5.1.2 Issues in ENF Testing

Specimen fabrication itself leads to a handful of issues that may be the underlying cause for the low G_{IIC} values gathered from test results. Initial fabrications of the panels included a 12.7 µm polyimide insert. No noticeable crack propagation was observed during tests. A bonding between the insert and the epoxy matrix of the 8552 material was revealed upon opening of the specimens after tests. To alleviate the issues due to epoxy-insert bonding, a final set of specimens were fabricated that included a baked on coating of release agent, Frekote (Manufacturer, City, State), onto the pre-crack insert. The addition of this release agent onto the insert allowed for successful testing, as seen in Figure 18. There is a distinct possibility, however, that the release agent may have propagated through the PMC and along the bond line of the specimen. Other researchers also observed such a phenomenon[30].

An issue within the Bluehill software was also observed before actual testing. According to the ENF ASTM standard[18], the 3-point bend test should be run at a set rate (between 0.1 and 0.8 mm/min) until reaching a preset loading, based upon initial compliance calibration calculations. This was not achievable with the Bluehill software; the system could only be run according to either load

rate, or load force. This meant that mixing the two, as required by the standard, could not be achieved. To circumvent this issue, extra specimens were included in tests; the loads for failure and compressive distances were recorded. From this information, set compressive distances were used for compliance calibration at the varying crack insert values. While this did achieve the intended result for compliance calibration, straying from the ASTM standard may have had unintended consequences for G_{IIC} calculations.

5.1.3 G_{IIC} Values

Despite the issues that may have arisen from fabrication or testing, or from issues within the use of the ENF standard itself, the fact remains that the tested specimens were all subjected to identical conditions as far as fabrication and testing are concerned. While the comparison between control specimen G_{IIC} values and other reported G_{IIC} values may have discrepancies, the G_{IIC} values observed from testing are still comparable.

Analysis of the SEM images showed that even with the addition of adhesives, the majority of the added adhesive sheared away cleanly from the SMA surface, adhering only to the PMC. Figures 13 and 14 reflect this, showing some delamination of the adhesive layer within the FM specimen versus no delamination of the Hysol specimen. This adhesive preference is further reflected in the G_{IIC} results, where the FM adhesive material performed better than the Hysol material, though both gave poorer results than the SMA control specimen.

As a final reflection of the instability of the bond within the test specimens, acoustic emissive signals for the majority of the tests were non-existent. Only in the first test of the control series was a significant amount of AE seen. The rest of the specimens generated a minimal amount of acoustic emissions during testing. The images from C-scans, optical microscopy, and SEM further can be coupled along with the lack of AE data to highlight the poor quality of the bond within the tested specimens, despite the use of adhesives to improve the bond.

6. Conclusion

The bond between ply layers in a CFRP composite is a focal point for failure in a variety of modes. Exploration of this failure mode for in-plane shear (mode II) produces a wide deviation of results. Despite the recent adoption of 3-point bend testing for ENF as an ASTM standard, the test itself has a history of varied results within set materials due to the unstable growth of the interlaminar crack during testing. The addition of SMA material between plies exacerbates this failure mode. The use of adhesives without any additional preparation of the SMA surfaces lowered interlaminar properties within the composite. The poor bonding was reflected in the results of SEM images of test specimens after failure. The lack of acoustic signals generated during testing was also an indicator that bonding was insufficient between SMA and PMC for in-plane shear. An increase in the bond between adhesive layers and SMA must be optimized via chemical or physical means before any significant gains in interlaminar fracture toughness can be achieved within a CFRP.

7. References

1. Araujo, CJ: Fabrication and static characterization of carbon-fiber-reinforced polymers with embedded NiTiNOL shape memory wire actuators*. Smart Materials and Structures* **2008,** *17*, 6.
2. Bollas, D: Stress Generation by shape memory alloy wires embedded in polymer composites. *Acta Materiala* **2007,** *55,* 5489-5499.
3. Parthenios, J: Adaptive composites incorporating shape memory alloy wires. *Composites: Part A* **2001**, *32*, 1735-1747.
4. Schrooten, J: Progress on Composites with Embedded Shape Memory Alloy wires*, Materials Transactions* **2002, 43,** 1-13.
5. Turner, T: Fabrication and Characterization of SMA hybrid composites*. Smart Structures and Materials* **2001,** *343,* 33-43.
6. Hisaaki, T; Elzbieta, P; Yoshihiro, E; Toshimi, S: Thermomechanical Properties of Shape-Memory Alloy and Polymer and Their Composites. *Mechanics of Advanced Materials and Structures* **2009,** *16*, 236-247.
7. Turner, T; Buehrle, R; Cano, R; Fleming, G: Modeling, fabrication, and testing of a SMA hybrid composite jet engine chevron concept. *Journal of Intelligent Material Systems and Structures* **2006,** *17,* 483-497.
8. Kim, C; Park, B-S; Goo, N-S: Shape Changes by Coupled Bending and Twisting of Shape-Memory-Alloy Embedded Composite Beams. *Smart Material Structures* **2002,** *11*, 519-526.
9. Ostachowicz, W: Dynamics and buckling of a multilayer composite plate with embedded SMA wires. *Composite Structures* **2000,** *48*, 163-167.
10. Poon, C; Zhou, L; Jin, W; Shi, S: Interfacial Debond of Shape Memory Alloy Composites. *Smart Material Structures* **2005,** *14,* 29-37.
11. Song, G; Kelly, B; Agrawal, BN; Lam, PC; Srivatsan, TS: Application of shape memory alloy wire actuator for precision position control of a composite beam*. Journal of Material Engineering Performance* **2000,** *9,* 330-333.
12. Lagoudas, DC: Modeling of a flexible beam actuated by shape memory alloy wires. *Smart Material Structures* **1997,** *6,* 265-277.
13. Hebda, DA; White, S.R.: Structural behavior of SMA composite beams. *Adaptive Material Systems* **1995,** *206*, 111-119.
14. Duering, TW; Melton, KN; Stockel, D: Engineering Aspects of Shape Memory Alloys*.* London: *Butterworth-Heinemann*, 1990.

15. J.S.N, Paine; C.A., Rogers: Review of multi-functional SMA hybrid composites materials and their applications. *Adaptive Structures and Composite Materials: Analysis and Application* **1994,** *54,* 37-45.
16. Xu, Y; Otsuka, K; Yoshida, H; Nagai, H; Oishi, R; Horikawa, H; Kishi, T: A New Method for Fabricating SMA/CFRP Smart Hybrid Composites. *Intermetallics* **2002,** *10,* 361-369.
17. Jang, BK; Kishi, T: Thermomechanical Response of TiNi Fiber-Impregnated CFRP composites. *Material Letters* **2005**, *59*, 2472-2475.
18. ASTM D7905: Standard Test Method for Mode II Interlaminar Fracture Toughness of Unidirectional Fiber-Reinforced Polymer Matrix Composites.
19. *Hexply 8552;* MSDS No. FTA 072e [Online]; Hexcel Composites, February 2013 http://www.hexcel.com/Resources/DataSheets/Prepreg-Data-Sheets/8552_eu.pdf (accessed May 2015)
20. *Loctite Hysol EA 9696*; ID No. AF9118512 [Online]; Henkel Adhesives, April 2007 http://hybris.cms.henkel.com/henkel/msdspdf?matnr=698917&country=US&language=EN (accessed May 2015)
21. *Cytec FM 377U;* ID No. AEAD-00014 [Online]; Cytect Adhesives, April 2010 http://www.cytec.com/sites/default/files/datasheets/FM_377_040710.pdf (accessed May 2015)
22. O'Brien, K; Johnston, W; Toland, G: Mode II Interlaminar Fracture Toughness and Fatigure Characterization of a Graphite Epoxy Composite Material. *NASA* TM-2010-216838, August 2010
23. Barrett, J.D; Foschi, R.O: Mode II stress-intensity factors for cracked wood beams. *Engineering Fracture Mechanics* **1977,** *9,* 371–378.
24. Russel, A.J; Street, K.N: Factors affecting the interlaminar fracture energy of graphite/epoxy laminates. Progress in science and engineering of composites. Proceedings of ICCM-IV, Tokyo, **1982,** 279-286.
25. Martin, R.H; Davidson, B.D.: Mode II fracture toughness evaluation using a four point bend, end notched flexure test. *Plastics Rubber and Composites* **1999,** *8,* 401– 406.
26. Wang, H; Vu-Khanh, T: Use of end-loaded-split (ELS) test to study stable fracture behaviour of composites under mode II loading. *Composites Structures* **1996,** *36,* 71–79.
27. Blackman, B.R.K; Kinloch, A.J; Paraschi, M: The determination of the mode II adhesive fracture resistance, G_{IIc}, of structural adhesive joints: an effective crack length approach. *Engineering Fracture Mechanics* **2005,** *72,* 877–897.

28. Wang, J; Qiao, P: Novel beam analysis of end notched flexure specimen for mode-II fracture. *Engineering Fracture Mechanics* **2004,** *71*, 219-231.
29. Martin, R: Interlaminar Fracture Characterization: A Current Review. *NASA Contractor Report* 187573 **1991**
30. Budzik, M; Jumel, J; Salem, N; Shanahan, M: Instrumented end notched flexure – crack propagation and process zone monitoring part I: Modelling and Analysis. *International Journal of Solids and Structures* **2013,** *50*, 297-309.
31. Budzik, M; Jumel, J; Salem, N; Shanahan, M: Instrumented end notched flexure – crack propagation and process zone monitoring part II: Data reduction and experimental. *International Journal of Solids and Structures* **2013,** *50,* 310-319.
32. Ouyang, Z; Guoqiang, L: Nonlinear interface shear fracture of end notched flexure specimens. *International Journal of Solids and Structures* **2009,** *46*, 2659-2668.
33. Renart, J; Vicens, J; Budhe, S; Rodriguez-Bellido, A; Comas, J; Mayugo, J; Costa, J: An automated methodology for mode II delamination tests under fatigue loading based on the real time monitoring of the specimen's compliance. *International Journal of Fatigue* **2016,** *82*, 6344-6642.
34. Prasad, B; Kumar, P: Analysis of composite ENF specimen using higher order beam theories. *Thin-Walled Structures* **2008,** *46*, 676-688.
35. Arrese, A; Mujika, F: Influence of bending rotations on three and four-point bend end notched flexure test. *Engineering Fracture Mechanics* **2008,** *75*, 4234-4246.
36. Boyano, A; De Gracia, J; Arrese, A; Mujika, F: Experimental assessment of an End Notched Flexure test configuration with an inserted roller for analyzing mixed-mode I/II fracture toughness. *Engineering Fracture Mechanics* **2016,** *163*, 462-475.
37. Sajith, S; Arumugam, V; Dhakal, H: Effects of curing pressure on Mode II fracture toughness of unidirectional GFRP laminates. *Polymer Testing* **2015,** *28*, 59-68.
38. Jagannathan, N; Chandra, A; Manjunatha, C: Onset-of-growth behavior of mode II delamination in a carbon fiber composite under spectrum fatigue loads. *Composite Structures* **2015,** *132*, 477-483.

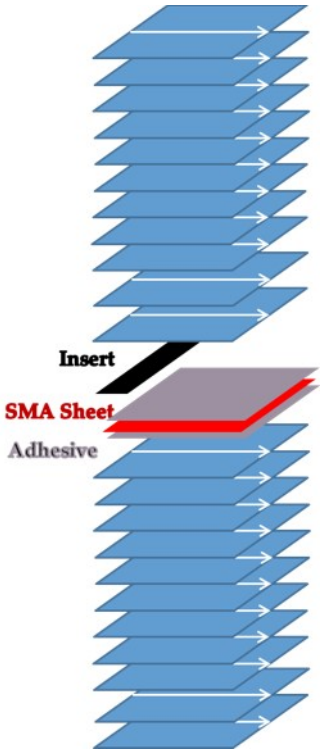

Figure 1 – Panel lay-up configuration for ENF testing: 11 plies on each side of SMA sheeting reinforced with thin film adhesive, non-stick insert included as pre-crack.

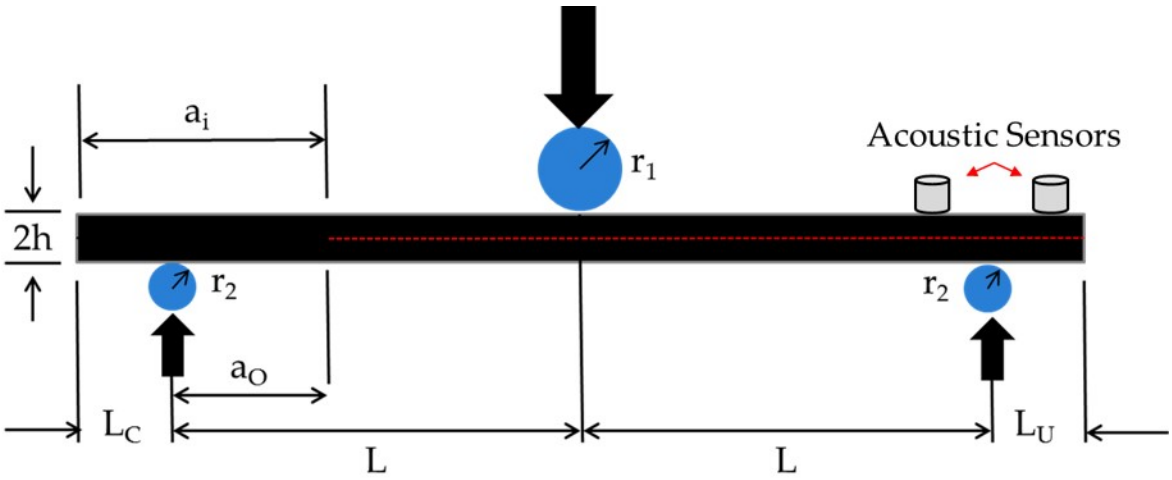

Figure 2. End-notched Flexure (ENF) 3-point bend test

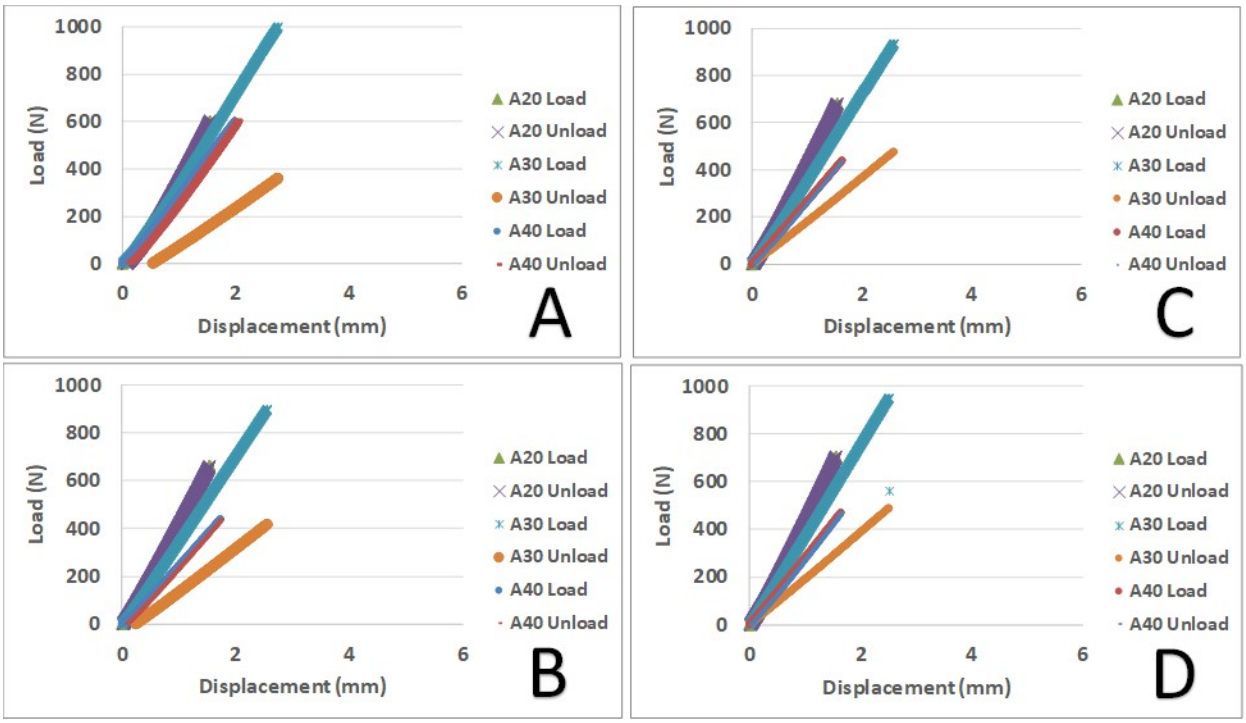

Figure 3. Compliance calibration and NPC Test results from Specimen Set 1: Control (No SMA). A: 1-1, B: 1-2, C: 1-3, D: 1-4

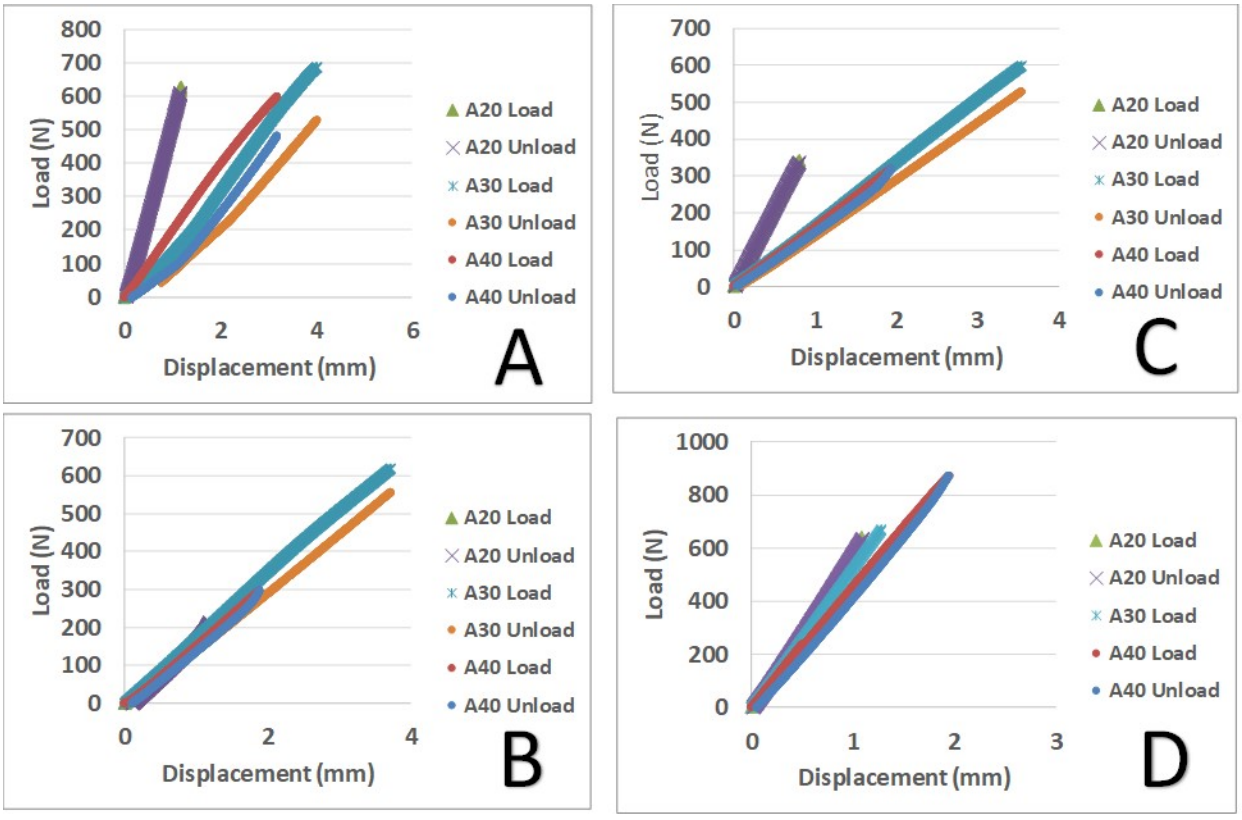

Figure 4. Compliance calibration and NPC Test results from Specimen Set 2: SMA (No adhesive). A: 2-1, B: 2-2, C: 2-3, D: 2-4

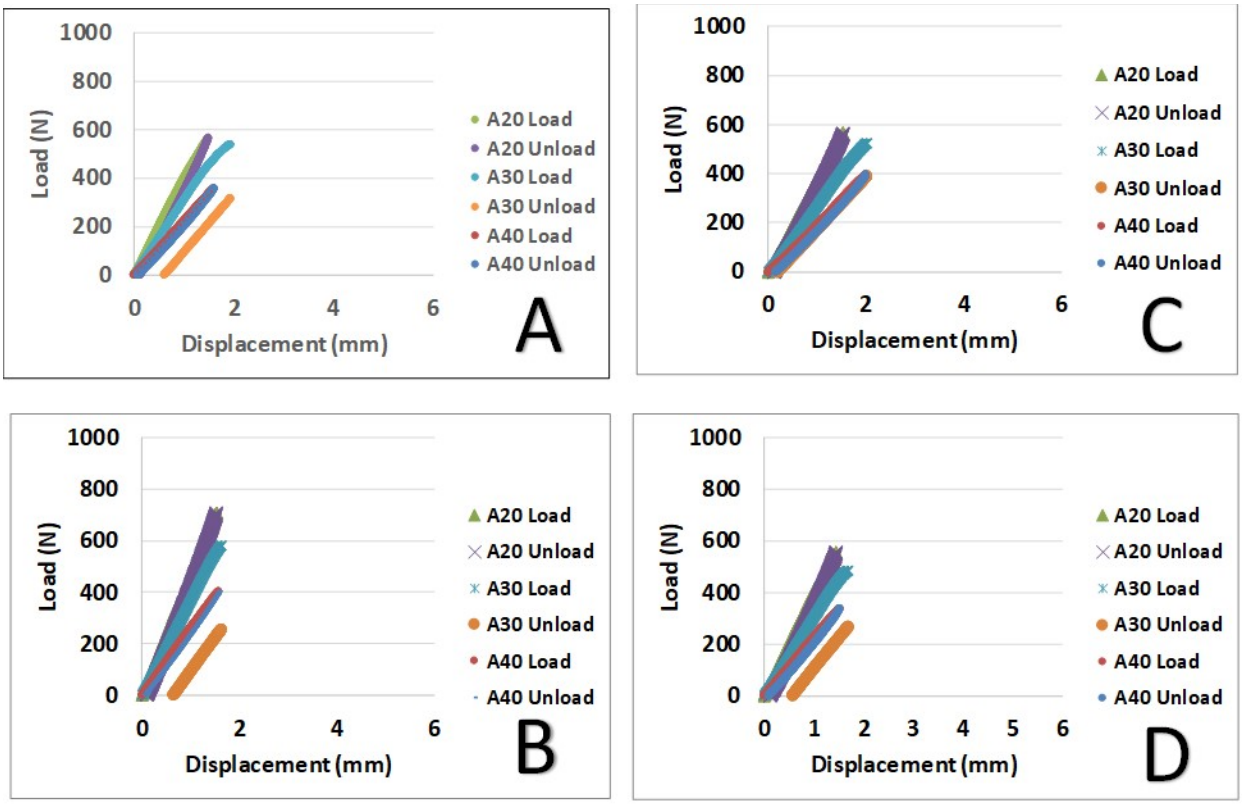

Figure 5. Compliance calibration and NPC Test results from Specimen Set 3: SMA (FM adhesive). A: 3-1, B: 3-2, C: 3-3, D: 3-4

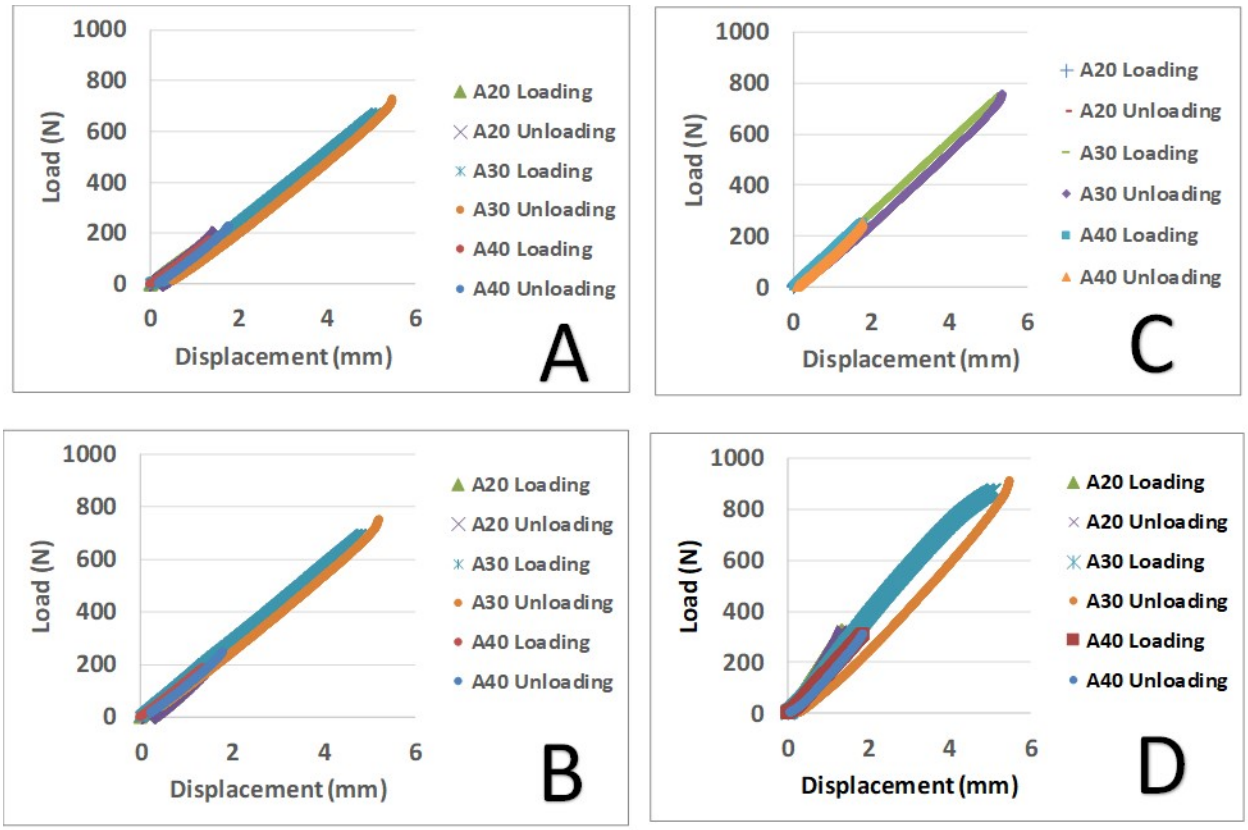

Figure 6. Compliance calibration and NPC Test results from Specimen Set 4: SMA (Hysol adhesive). A: 4-1, B: 4-2, C: 4-3, D: 4-4

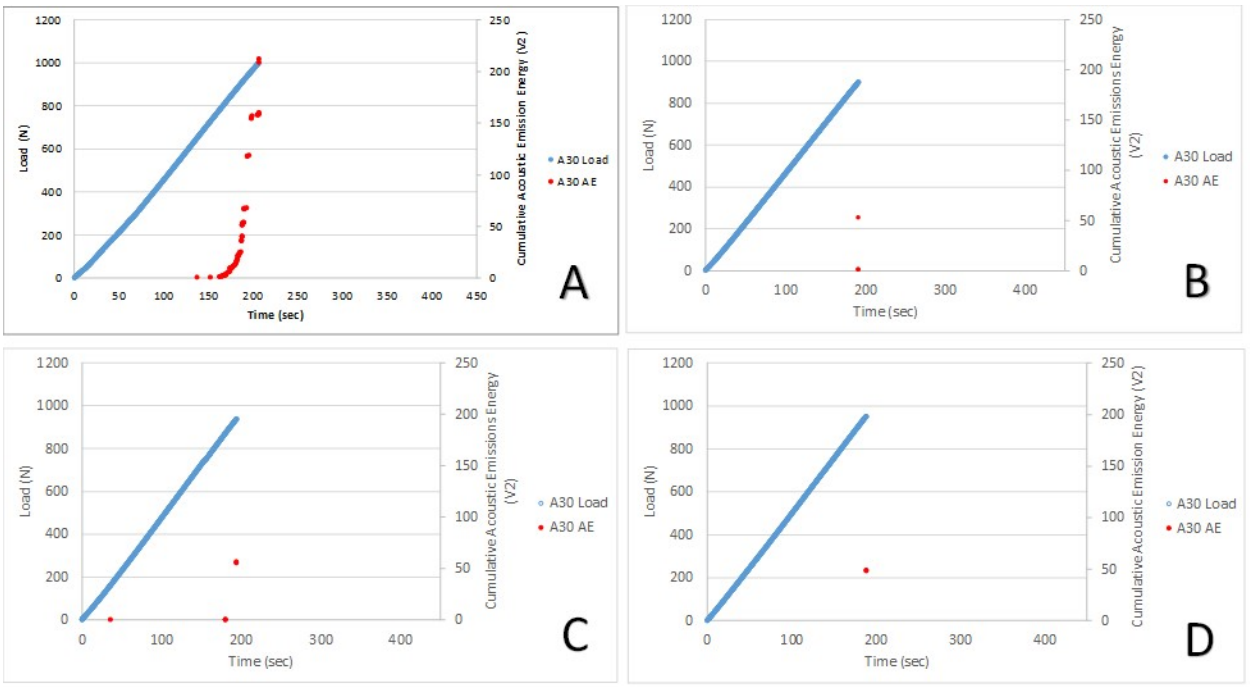

Figure 7. Cumulative Acoustic Emissions plotted alongside Load for Control Series. A: 1-1, B: 1-2, C: 1-3, D: 1-4

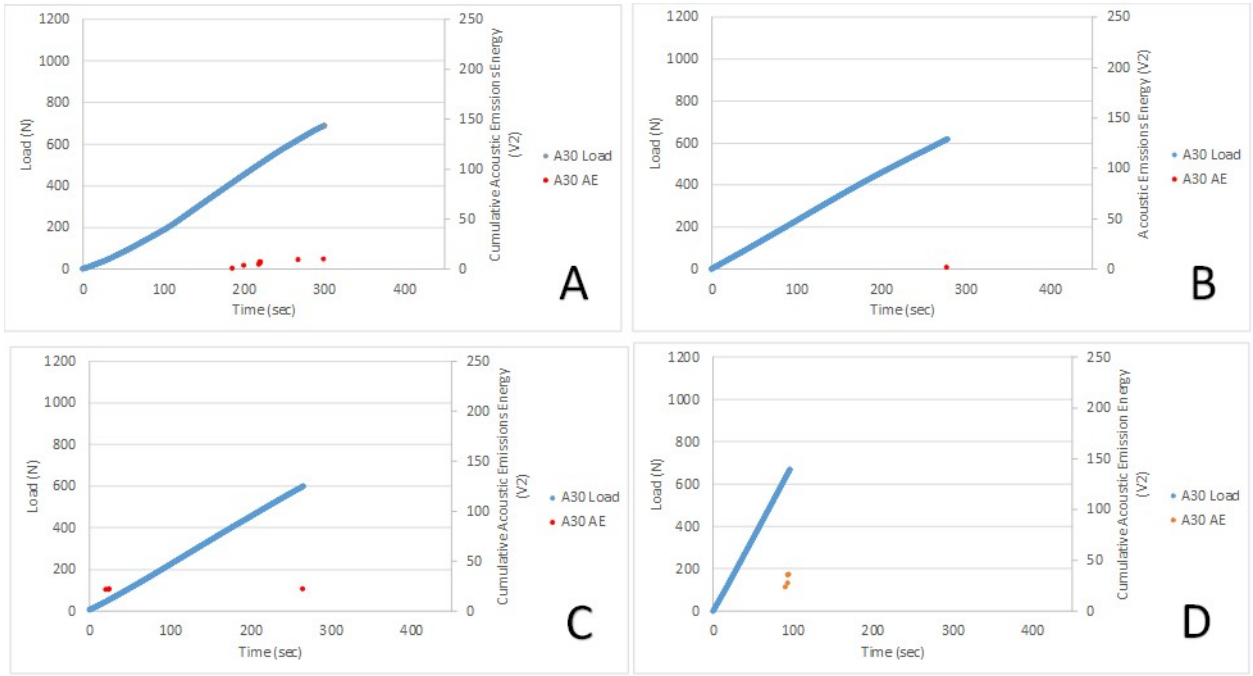

Figure 8. Cumulative Acoustic Emissions plotted alongside Load for SMA Control Series. A: 2-1, B: 2-2, C: 2-3, D: 2-4

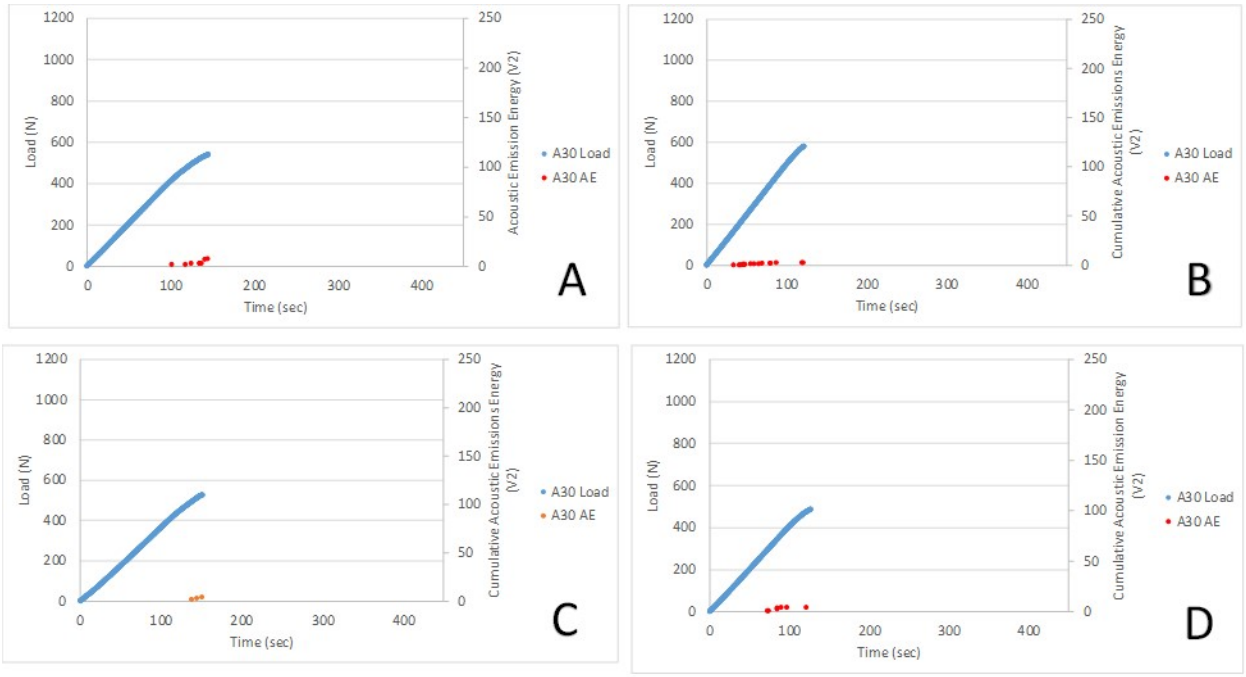

Figure 9. Cumulative Acoustic Emissions plotted alongside Load for SMA/FM Series. A: 3-1, B: 3-2, C: 3-3, D: 3-4

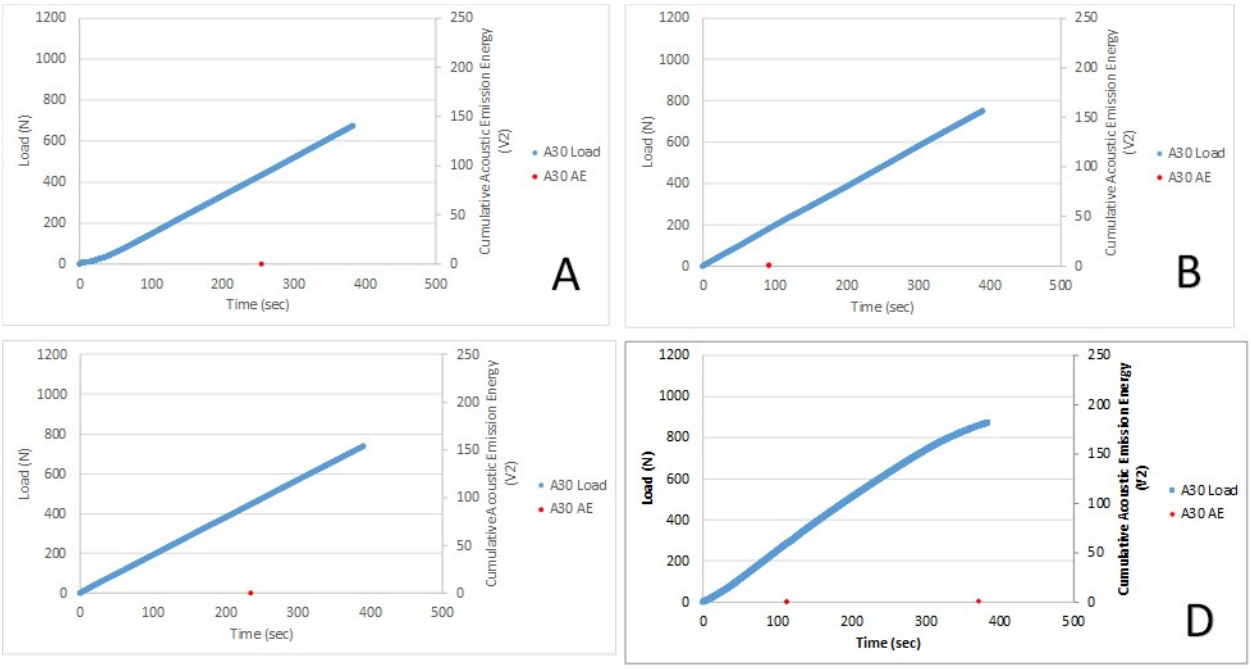

Figure 10. Cumulative Acoustic Emissions plotted alongside Load for SMA/Hysol Series. A: 4-1, B: 4-2, C: 4-3, D: 4-4

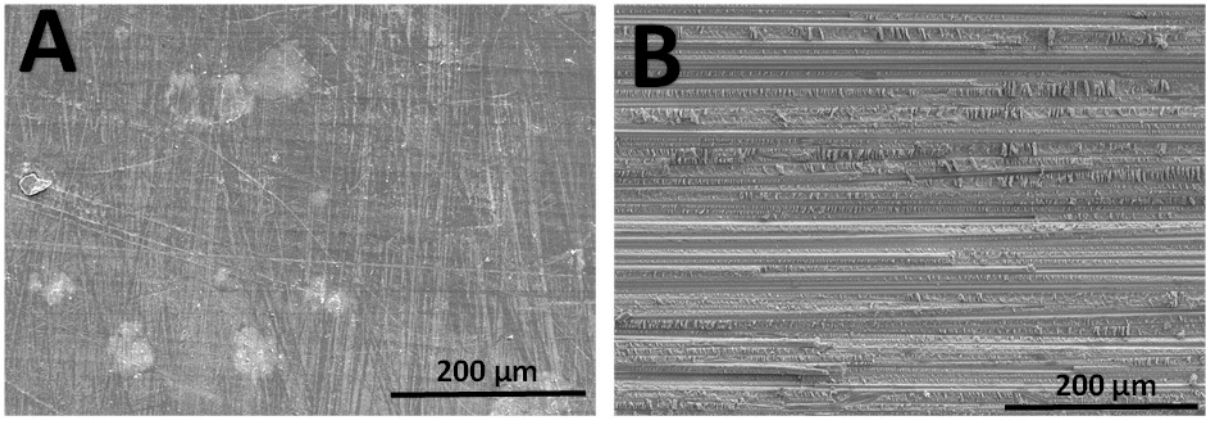

Figure 11. Scanning Electron Microscopy of the pre-crack (A) and crack propagation (B) sections of control series specimen 1-1.

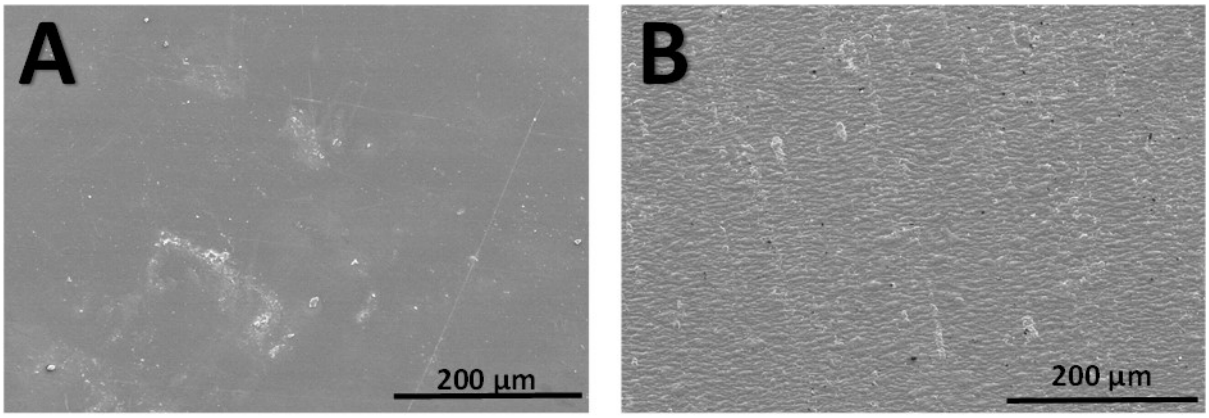

Figure 12. Scanning Electron Microscopy of the pre-crack (A) and crack propagation (B) sections of SMA control series specimen 2-2.

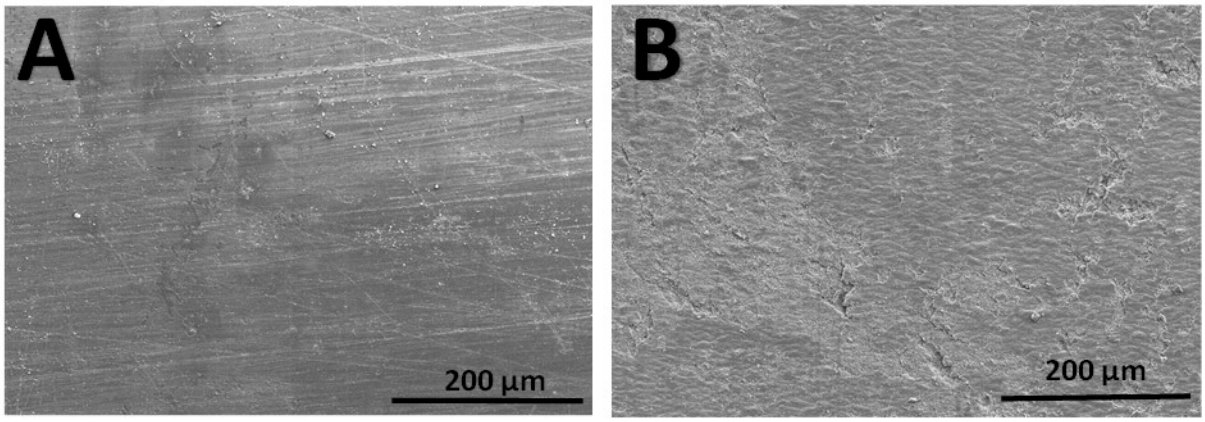

Figure 13. Scanning Electron Microscopy of the pre-crack (A) and crack propagation (B) sections of SMA/FM series specimen 3-2.

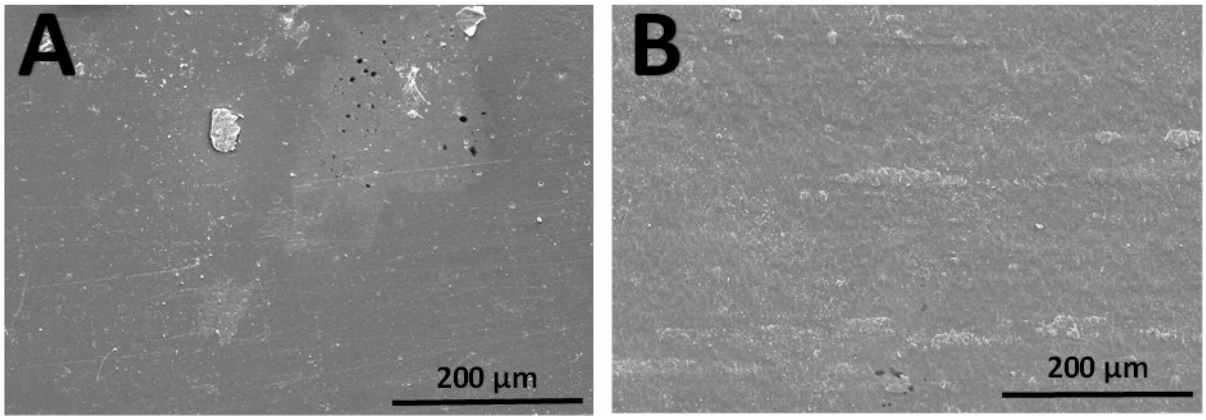

Figure 14. Scanning Electron Microscopy of the pre-crack (A) and crack propagation (B) sections of SMA/Hysol series specimen 4-1.

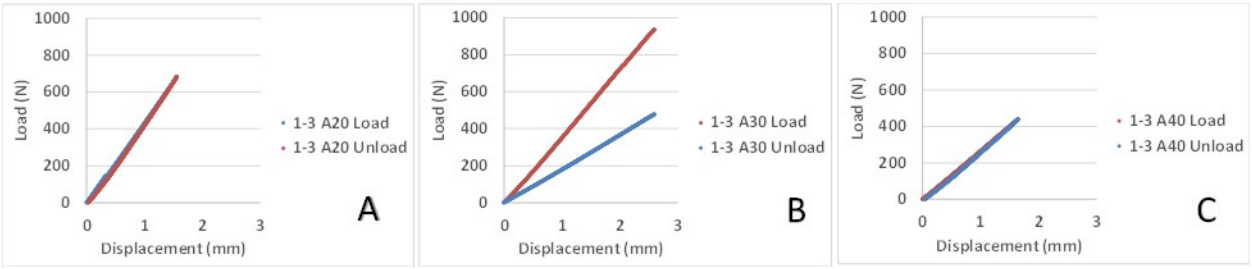

Figure 15. Compliance Calibration load displacement plots for specimen 1-3: A_0 = 20mm (A), A_0 = 30mm (B), A_0 = 40 mm (C)

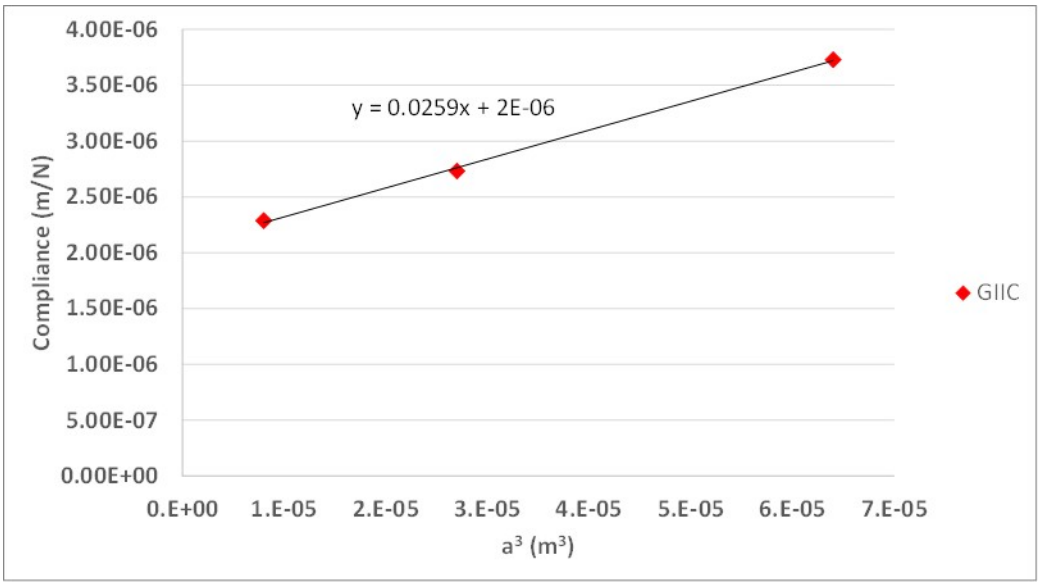

Figure 16. Compliance vs Crack Length plots for Specimen 1-3 – A = 2E-06, m = 0.026

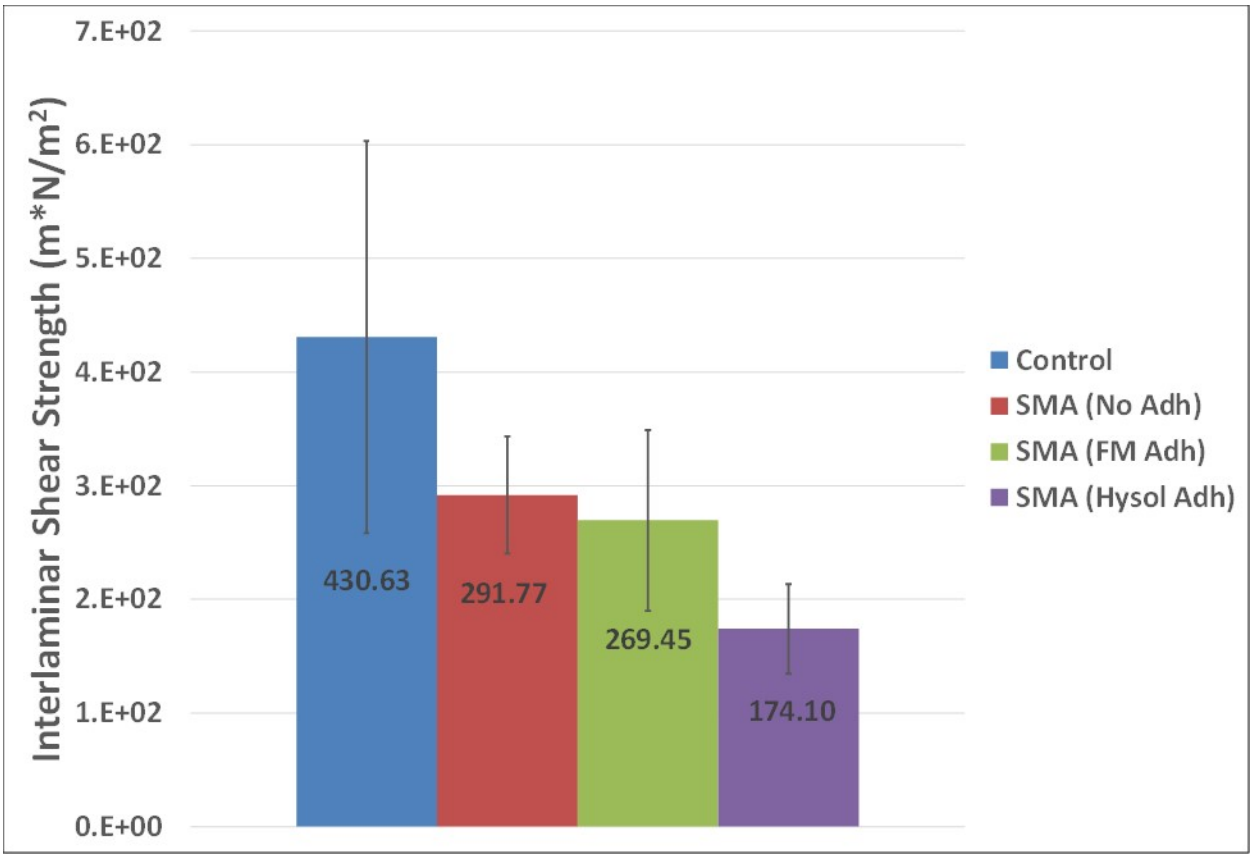

Figure 17. Fracture Toughness Averages for ENF Testing

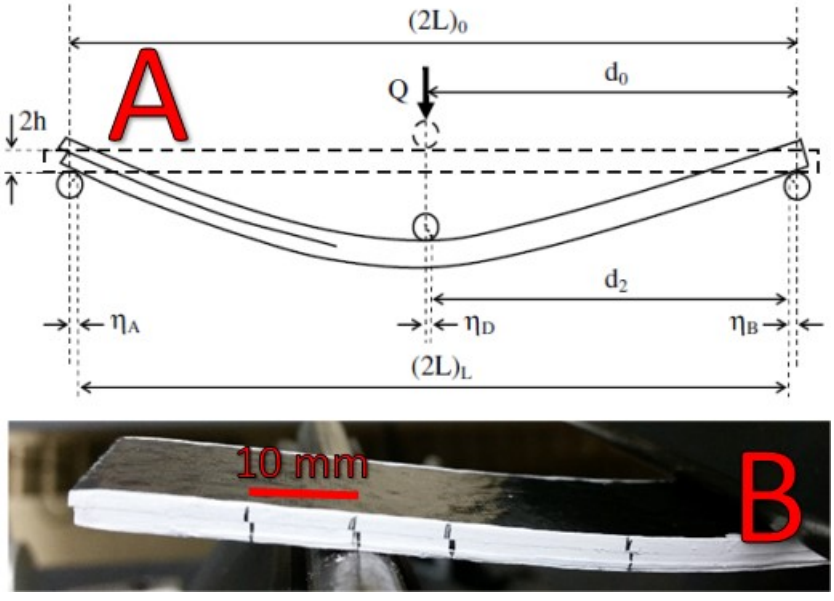

Figure 18. Theoretical crack propagation of ENF specimen (left) and actual crack propagation of tested specimen (right)